Experimental and model investigation of the time-dependent 2-dimensional distribution of binding in a herringbone microchannel†

Jennifer O. Foley,‡[a] Afshin Mashadi-Hossein,§[a] Elain Fu,[a] Bruce A. Finlayson[b] and Paul Yager*[a]

Received 5th September 2007, Accepted 15th January 2008
First published as an Advance Article on the web 21st February 2008
DOI: 10.1039/b713644g

A microfluidic device known to mix bulk solutions, the herringbone microchannel, was incorporated into a surface-binding assay to determine if the recirculation of solution altered the binding of a model protein (streptavidin) to the surface. Streptavidin solutions were pumped over surfaces functionalized with its ligand, biotin, and the binding of streptavidin to those surfaces was monitored using surface plasmon resonance imaging. Surface binding was compared between a straight microchannel and herringbone microchannels in which the chevrons were oriented with and against the flow direction. A 3-dimensional finite-element model of the surface binding reaction was developed for each of the geometries and showed strong qualitative agreement with the experimental results. Experimental and model results indicated that the forward and reverse herringbone microchannels substantially altered the distribution of protein binding (2-dimensional binding profile) as a function of time when compared to a straight microchannel. Over short distances (less than 1.5 mm) down the length of the microchannel, the model predicted no additional protein binding in the herringbone microchannel compared to the straight microchannel, consistent with previous findings in the literature.

Introduction

Microfluidic technologies have the potential to change the medical diagnostic paradigm by serving as an enabling technology that will take medical tests from a large centralized hospital laboratory to the side of the patient.[1–5] Microfluidic assays have several advantages over conventional large-scale assays that make them an appropriate technology for this application; these advantages include: a reduction in sample and reagent volumes, the potential to reduce the size of the instrumentation to that suitable for point-of-care diagnostic equipment, the potential to use inexpensive and disposable polymeric materials for microfluidic device fabrication, and a reduction in the amount of waste generated.[6–8]

Given the advantages of microfluidic diagnostics, numerous microfluidic assay formats have been developed. In one common assay format, the surface of a microchannel is functionalized with a capture molecule that will bind to an analyte from the sample solution (Fig. 1a). The binding of the analyte is monitored over time and can be used to quantify the analyte concentration. A major challenge in the development of a rapid microfluidic medical diagnostic that uses this assay format is to increase the transport of analyte to the surface. Laminar flow dominates in microfluidic channels, and thus the surface binding reaction is often diffusion-limited.[9–14]

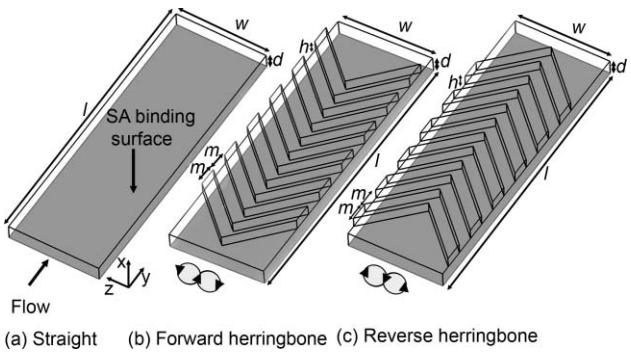

Fig. 1 Schematic of the microchannel geometries for the (a) straight, (b) forward herringbone and (c) reverse herringbone configurations. The direction of flow is indicated in (a). The direction of the two recirculating streams for the (b) forward herringbone microchannel and (c) reverse herringbone microchannel are indicated at the inlet of the devices. For the modeled microchannel, $d = 82$ μm, $h = 56$ μm, $w = 500$ μm, $m = 100$ μm and $l = 1.5$ mm. The biotin-functionalized gold surface to which streptavidin (SA) from solution will bind is indicated in (a).

Several methods have been explored to increase the transport of the analyte to the binding surface. One method is to increase the flow rate of the sample solution. However, this method consumes more analyte, and the increased flow rate and pressure could also lead to device failure. Another method is to implement an active mixing method, *i.e.* a method that requires external actuators, to mix the bulk solution and replenish the concentration of analyte near a binding surface, overcoming mass-transport limitations. Pulsed peristaltic pumping,[13–17]

[a]*Department of Bioengineering, University of Washington, Seattle, WA, USA. E-mail: yagerp@u.washington.edu; Fax: +1 (1)206 616 3928; Tel: +1 (1)206 543 6126*
[b]*Department of Chemical Engineering, University of Washington, Seattle, WA, USA; Fax: +1 (1)206 685 3451; Tel: +1 (1)206 685 1634*

† Electronic supplementary information (ESI) available: Computational results of the fluid mechanics, analysis of the surface binding profiles of streptavidin, and the governing equations of the model. See DOI: 10.1039/b713644g

‡ Present address: Department of Bioengineering, University of Pennsylvania, Philadelphia, PA 19104, USA
§ Present address: NanoString Technologies, Seattle, WA, USA. Fax: +1 (1)206 378 6288; Tel: +1 (1)206 378 6288

electrothermal stirring,[12] magnetic beads,[18] centrifugal mixing,[19] and pulsed air-driven bladders[20] have been used to stir the fluid in a range of microfluidic assays including DNA microarrays,[13–17,19–21] ELISAs[18] and immunoassays.[11,12,20] These methods typically increase the rate of binding or the sensitivity of the assay by a factor ranging from two to ten.

However, external actuators add complexity, cost and increased power consumption to a medical diagnostic. Therefore, a passive method to increase the rate of binding of analyte to the surface would be more suitable and cost-effective. There are several examples in the literature in which passive mixers—microfluidic channels in which the geometry of the channel serves to mix the solution[22]—have been incorporated in microfluidic assays.

In one example, Vijayendran *et al.*[23] incorporated a serpentine microfluidic mixer in a microfluidic assay. A two-fold increase in the initial binding rate of a protein, an IgG, to the surface as measured by surface plasmon resonance (SPR) spectroscopy was reported. The authors suggest that the "unstirred" region at the wall of the device prevents the mixing of the solution at the surface, thereby resulting in little to no difference in the concentration of IgG near the surface and in turn a relatively small increase in the rate of binding of IgG. However, only a limited range of flow rates was explored and the detection method averaged the signal over the entire channel, thereby ignoring localized variations in surface binding.

Another example of a passive microfluidic mixer that has been incorporated into microfluidic surface reaction assays is the herringbone micromixer (Fig. 1b). This microfluidic geometry, first presented by Stroock *et al.*,[24] imposes a secondary flow that has been shown to reduce the total time to achieve mixing of solutions in the bulk of the microchannel. The herringbone microstructures, which sit above a base microchannel, alter the pressure fields on the fluid and generate recirculation perpendicular to the primary flow direction. In the herringbone geometry, two spiraling flows (clockwise and counter-clockwise) on either side of the herringbone point are created. A related mixer geometry, the grooved microchannel, which has slanted grooves on top of the microchannel and mixes the solution based on considerations similar to those for the herringbone microchannel, has also been developed[25,26] and applied to microfluidic surface assays.

Yoon *et al.*[10] incorporated a grooved passive mixer to improve a surface electrochemical reaction (conversion of ferrocyanide to ferricyanide). The electrochemical reaction occurred at the sidewalls of the device, and the measurement of the conversion was completed off-line at a fixed endpoint. The microfluidic mixer increased the conversion efficiency of the reaction by ten to forty percent depending on the flow rate. Golden *et al.*[9] incorporated a passive mixer that was a combination of a herringbone microchannel and a grooved microchannel in a microfluidic assay and reported a 26% improvement in the assay results when averaging the signal along the length of the channel. The authors also explored the spatial variation in the binding signal in 1 dimension, *i.e.* the length of the channel, and demonstrated greater increases in the binding signal of the mixer microchannel over a straight microchannel with increasing downstream distance. However, the spatial resolution of their method was not sufficient to reveal fine-grained features of the binding patterns of the mixer microchannels. To obtain a more detailed understanding of the operation of the herringbone structures, an investigation of the 2-dimensional binding profile of the reaction surface as a function of time is necessary.

In this work, herringbone microchannels were used to house a microfluidic assay (Fig. 1b), and the resulting 2-dimensional binding profiles as a function of time were evaluated and compared to that for a straight microchannel (Fig. 1a); data from both experiments and computational modeling are compared here. Note that the term "herringbone microchannels" is used to distinguish the current devices containing symmetric herringbone structures from the original herringbone "micromixers" of Stroock *et al.*[24] that consisted of alternating sets of offset herringbone structures. The purpose of this research is to determine if the recirculation influences the spatio-temporal binding of a model protein to a binding surface and whether it increases the rate of binding to the surface. The binding of a model protein, streptavidin (SA), to its surface immobilized ligand, biotin, was monitored using SPR imaging—a surface-sensitive technique that monitors changes in refractive index near a surface.[27–29] This method, unlike conventional SPR spectroscopy, can monitor localized increases in surface binding as it occurs, providing a 2-dimensional profile of the binding of the protein as a function of time. This work compares the herringbone geometry in the forward (Fig. 1b) and reverse (Fig. 1c) configurations, as well as the straight channel configuration (Fig. 1a). A three-dimensional computational model incorporating the mass transport and surface binding reaction of SA to the binding surface was developed; this is the first attempt to model a surface binding reaction in a herringbone microchannel. Experimental and model results are in good qualitative agreement.

A computational model of the microfluidic system will yield important insights into the physical processes occurring in the assay and may serve as a tool for further optimization and exploration into novel assay designs. The surface binding reaction in the model was governed by eqn (1) and (2).

$$c_{SA} + \theta \underset{k_{des}}{\overset{k_{ads}}{\rightleftharpoons}} c_s \tag{1}$$

$$\frac{dc_S}{dt} = k_{ads} c_{SA} (\theta_0 - c_s) - k_{des} c_s \tag{2}$$

Here c_{SA} is the streptavidin concentration in the bulk of the microchannel, c_s is the surface concentration of bound streptavidin, θ_0 is the initial surface concentration of streptavidin binding sites, θ is the surface concentration of streptavidin binding sites and k_{ads} and k_{des} are the adsorption and desorption kinetic parameters. Nelson *et al.*[30] and Jung *et al.*[31] have extensively characterized the SA–biotin system used in this work. Several key parameters required by the model had been measured experimentally, making this system conducive to modeling.

Materials and methods

Experimental methods

Chemicals and reagents. Streptavidin (US Biologics, MA, USA) was diluted in phosphate-buffered saline (PBS, pH 7.4)

(Sigma, St. Louis, MO). Deionized water was used throughout the work. Biotinylated alkyl thiol (BAT) (Iris BioTECH GmbH, Germany—custom synthesis) and ethylene glycol thiol ($n = 4$) (Prochimia, Sopot, Poland) were diluted in absolute ethanol.

Microfluidic device fabrication. The microchannels were constructed using established soft lithography methods.[32,33] The mask for the herringbone microchannel required two layers of photolithography. High resolution transparencies served as the photolithography masks. The masks were drawn using AutoCAD 98 (Microsoft, Redmond, WA) and Adobe Illustrator 10 (Adobe Systems Inc., San Jose, CA). The first mask generated the rectangular base of the microchannel. The second mask generated the herringbone microstructures. A negative photoresist, SU8 (MicroChem, Newton, MA), was spun (Solitec Spinner, Milpitas, CA) onto clean, three-inch silicon test wafers (Silicon Sense, Nashua, NH). An infrared contact aligner (AB-M, San Jose, CA) exposed the wafers to ultraviolet light. The depth of the SU8 features were measured with a P15 surface profilometer (Tencor, San Jose, CA). Silicone tubing (Cole Parmer, Vernon Hills, IL) was glued onto the SU8 molds with DuCo Cement (Devcon, Riviera Beach, FL) to generate inlets and outlets. Sylgard 184 prepolymers (Dow Corning, Midland, MI) were dispensed at a 10 : 1 ratio of polymer to curing agent onto the SU8 molds to generate the polydimethylsiloxane (PDMS) devices.

In initial studies, bubbles repeatedly formed within the herringbone microstructure. To overcome this technical issue, the PDMS devices were activated in oxygen plasma to create a more hydrophilic surface (oxygen pressure 30 psi for 1 min at 600 W in a Plasma Preen II 973, Plasmatic System, Inc., North Brunswick, NJ). During the plasma activation, the PDMS device was masked so that only the microchannel itself was exposed to the oxygen plasma.

Gold-coated slide preparation. A 1 nm layer of chromium (for adhesion) and a 45 nm layer of gold were electron-beam deposited (CHA 600, CHA Industries, Fremont, CA) onto clean glass microscope slides (Fisher Scientific, Pittsburgh, PA). To avoid leaks at an interface of the PDMS and gold surface functionalized with thiols, gold was deposited on the glass slide only in regions defined by the microchannel using stainless steel masks (Precision Image Corporation, Bothell, WA). The gold-coated glass substrates were cleaned under oxygen plasma (oxygen pressure 30 psi) for 1 min (Plasma Preen II 973, Plasmatic System, Inc., North Brunswick, NJ) at 600 W. The oxygen-plasma-cleaned slide was patterned with thiols using a technique based on capillary action and described elsewhere.[34] Briefly, a mask was cut from a 250 μm sheet of Mylar (Fralock, Canoga Park, CA, USA) using a CO_2 laser (M25, Universal Laser System, Inc., Scottsdale, AZ). The mask was placed onto the slide using an alignment jig to ensure that thiols were deposited only in the region of the gold surface that would be within the microchannel. A 0.5 mM solution of BAT–HS-PEG (10% BAT, 90% HS-PEG) was introduced into a hole previously cut in the Mylar mask. Capillary forces wicked the solution underneath the mask and the thiol solution was allowed to evaporate. A 0.5 mM solution of HS-PEG was then pipetted onto the exposed regions of gold outside of the masked region, allowed to evaporate, and the mylar mask was removed. HS-PEG has been shown in the literature to significantly reduce non-specific binding. The slide was thoroughly rinsed in ethanol for one minute to remove any excess thiols and then dried with nitrogen gas. The oxygen-plasma-activated PDMS microchannel was then aligned with and placed on top of the gold substrate.

SPR imaging experiments. A home-built wavelength-tunable SPR microscope described in detail elsewhere[29] was used to collect the experimental data. Briefly, a 150 W quartz halogen lamp (Dolan–Jenner, Lawrence, MA) was coupled to a multi-fiber light pipe (Edmund Industrial Optics, Barrington, NJ) and sent through a 400 μm pinhole (Edmund Industrial Optics, Barrington, NJ). An achromatic lens (Edmund Industrial Optics, Barrington, NJ) collimated the light, which then passed through a polarizer (Edmund Industrial Optics, Barrington, NJ) and a 905 nm interference filter (Edmund Industrial Optics, Barrington, NJ). The interference filter was mounted on a stage (Newport Corporation, Irvine, CA) which rotated the filter face with respect to the beam of incident light. As the filter was tilted off-axis, the light passed by the filter was blue-shifted, enabling wavelength tuning. The light then passed through a custom-ground BK7 prism (Matthew's Optical, Poulsbo, WA) to the gold-coated substrate and sample (angle of incidence of approximately 64.8°). The reflected light was focused with an achromatic lens (Edmund Industrial Optics, Barrington, NJ) onto a charge-coupled device (CCD) detector (Retiga EX, Qimaging, Burnaby, Canada). Custom-coded data acquisition and control programs written in the Labview programming environment (National Instruments, Austin, TX) automated the collection of the images and the rotation of the interference filter and the polarizer.

SPR images were collected as a 40 nM solution of streptavidin in PBS was introduced to the PDMS device at a flow rate of 50 nL s^{-1} using a computer-controlled syringe pump (MicroFlow system, Micronics, Redmond, WA). This flow rate corresponded to a Reynolds number of 1.11×10^{-1} and a Peclet number of 1.48×10^{3} (where the characteristic depth was the depth of the base microchannel, *i.e.* 82 μm). Initially, buffer filled the microchannel. A six-port injection valve (Upchurch Scientific, Oak Harbor, WA) introduced the solution of streptavidin from the 2 mL sample loop to the microchannel. The interference filter position, 22° from normal, was chosen such that the imaging wavelength was located at the base of the linear region of the SPR curve (data not shown). The integration time was approximately 0.5 s. Images were collected at an interval of 15 or 30 s. The SPR data were analyzed using custom-coded programs written in the Labview programming environment (National Instruments Corp., Austin, TX). To calculate the change in reflectivity, a dark image was subtracted pixel by pixel from each image. The dark-corrected TM image (polarization of light which excites surface plasmons) was then divided pixel by pixel by a dark-corrected TE image (polarization of light which does not excite surface plasmons) to normalize for nonuniform illumination across the instrument field of view. Finally, a correction factor specific to the operation of the instrument design used in this study was applied as described elsewhere.[35] Three replicates were completed. The SPR difference images were processed by subtracting the initial image of the channel, filled with a buffer solution, from the image for a given time point.

Computational simulations

All computational simulations were completed with the commercially-available finite-element method software, COMSOL® (Version 3.3, Comsol, Inc., Burlington, MA) on a G5 PowerMAC with 8 GB of RAM and a dual 2.5 GHz processor. The models built upon a simple two-dimensional adsorption example in the model library of COMSOL®,[36] and have been applied to other microfluidic assay systems.[37] Each three-dimensional geometry (Fig. 1) contained a streptavidin binding surface. The initial conditions specified that the concentration of streptavidin was zero within the microchannel and that no streptavidin was bound to the surface. First, the steady-state Navier–Stokes mode was solved to obtain the velocity profile within the microchannel. Then, using this solution, the transient convection–diffusion and surface binding modes were solved simultaneously (*i.e.* the weak-boundary mode of COMSOL® solved the surface binding reaction and coupled it to the flux of antibody through the binding surface in the boundary conditions of the convection–diffusion mode).

In the model, a 40 nM solution of streptavidin was introduced to the microchannel at a flow rate of 5 nL s^{-1} which corresponded to a Reynolds number of 1.11×10^{-2} and a Peclet number of 1.48×10^{2}. For these calculations, the characteristic dimension was chosen as the depth of the base microchannel (d). The diffusion coeffient for streptavidin was 7.4×10^{-11} m^2 s^{-1}.[38] The surface concentration of streptavidin binding sites (3.99×10^{-8} mol m^{-2}) was based on experimentally measured values.[30,31] The k_{ads} (4.0×10^{7} M^{-1} s^{-1}) and k_{des} (3.0×10^{-6} s^{-1}) were based on an experimentally estimated value of k_{des}[31] and an assumed equilibrium constant of 1.3×10^{13} M^{-1} which falls within the range of the experimentally measured equilibrium constants for the binding of streptavidin and biotin in solution.[39] The model assumed that the binding of streptavidin to the surface only occurred between one immobilized biotin molecule and one streptavidin binding pocket. Multiple biotin interactions for a single streptavidin molecule were not considered in the model. The viscosity (1.0×10^{-3} kg m^{-1} s^{-1}) and density (1.0×10^{3} kg m^{-3}) of the solution were based on experimentally measured values for water at room temperature.[40]

Results and discussion

The choice of an appropriate control microchannel is critically important for assessing the influence of a herringbone microchannel on a surface binding reaction in a microfluidic protein assay. Given its precedence in the literature,[9,10] a straight microchannel (Fig. 1a) with a channel depth (d in Fig. 1a) equal to the base channel of the herringbone microchannel was selected as the control microchannel to the forward (Fig. 1b) and reverse (Fig. 1c) herringbone configurations investigated. Since a reduction of the sample volume is very important in the development of point-of-care diagnostics, the volumetric flow rate (rather than an average velocity) was kept the same in all three devices. (See the ESI† for model results of an alternative control geometry, the rectangular microchannel, in which microstructures of the same depth and width as the herringbone structures but positioned perpendicular to the initial direction of flow, rather than at an acute angle, are located above a base channel.)

There are several important differences between the experimental and the model systems that should be noted. First, the experimental system contains a 35 μL dead volume upstream of the binding surface that was not incorporated in the model due to memory constraints. Therefore, the influence of dispersion is more significant in the experimental system than in the model system and the time points between the model and experimental results do not directly correspond. Second, high flow rates (producing large Peclet numbers) are difficult to model without encountering convergence problems.[41] As a result, the modeled flow rate was 5 nL s^{-1}, while the flow rate for the experimental system was constrained to be no lower than 50 nL s^{-1}. Finally, the surface binding of SA was monitored in a large area that extended 5.6 mm downstream from the leading edge of the binding surface, while the model only examined SA binding to 1.5 mm downstream of the start of the binding surface (due to memory constraints). With the introduction of more affordable, larger-memory computer systems and/or microfluidic valves, these limitations could be overcome. However, even with these differences, the model results show strong qualitative correlation with the experimental results.

Surface binding profiles of SA

SPR difference images for the herringbone microchannel show dramatic spatial and temporal variations in binding across the SA binding patch (Fig. 2). Specifically, there is a steep reduction in the amount of bound SA at the midline of the microchannel (10 min and 20 min) that only "fills in" at later times (30 min). In addition, the experimental results indicate subtle variations in the binding of SA down the length of the microchannel that are the most notable at the 10 min timepoint. Visualization of the latter is limited due to characteristics of the SPR imaging instrument used in this study, namely the y-dimension is foreshortened and the area of "best" focus is small compared to the size of the experimental binding patch being monitored.

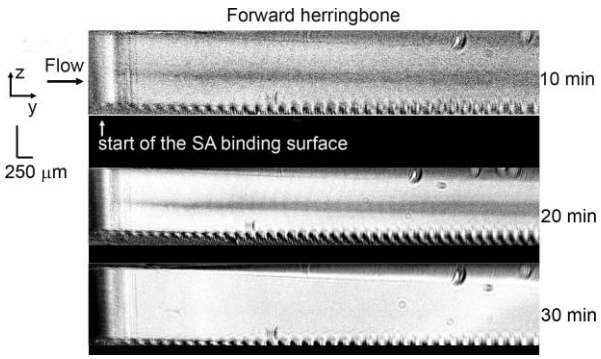

Fig. 2 Experimental surface concentration profile of bound SA over time in a forward herringbone microchannel. SPRM difference images were created by subtracting the image at the time indicated from the initial image in which only PBS buffer was present. Each image was contrast-enhanced for viewing purposes. Note the qualitative agreement between these experimental results and the model results presented in Fig. 4. Specifically, there exists a region of lower surface concentration along the midline of the channel.

The SPR difference images for the reverse herringbone and straight microchannels show very different binding patterns compared to the herrringbone microchannel (Fig. 3). Both show relatively uniform binding across the binding patch at 20 min. Note that there is slightly more binding along the midline of the channel, compared to near the sidewalls, for the reverse herringbone microchannel, while there is more binding in the upstream region of the binding patch for the straight microchannel.

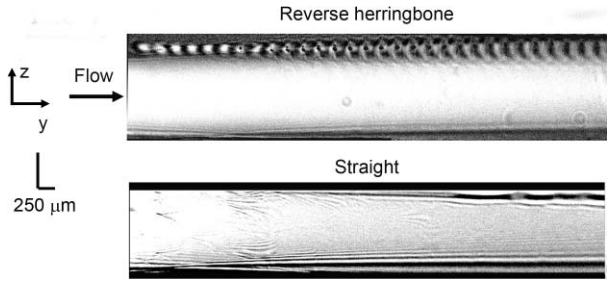

Fig. 3 Experimental surface concentration profile of bound SA in the reverse herringbone microchannel and straight microchannel at time = 20 min. SPRM difference images created by subtracting the image at 20 min from the initial image in which only PBS was present. Each image has been contrast-enhanced for viewing purposes. Note the uniform surface concentration in both these microchannels, in contrast to the results for the forward herringbone microchannel of Fig. 2 at the same time.

Model results for the three channel configurations (Fig. 4) demonstrate fine-grained spatial and temporal variations in binding and show good qualitative agreement with the experimental results. The model results for the straight channel (leftmost column in Fig. 4) show that the majority of the surface binding of SA occurs during the first five minutes of the assay and in the first 300 μm of the surface. This spatial variation in the binding profile indicates that the assay is operating in the mass-transport-limited regime and that a reduction in the time of the assay necessitates overcoming the sharp reduction in the SA binding near the start of the binding surface. The model results also indicate that there is a reduction in the amount of bound SA very near the sidewalls. This can be attributed to the reduced fluid velocity of the no-slip condition at the wall of the device. In those areas, the surface binding reaction is limited by mass-transport, as the SA must reach the binding surface by diffusion and the concentration of SA near the surface must be replenished by diffusion.

The model results of the herringbone microchannel (middle column in Fig. 4) highlight the two features observed in the experimental surface binding profile of SA. First, there is the marked reduction in the amount of SA bound at the midline of the microchannel (z-dimension). The model results indicate that at later times the area along the midline "fills in" (also in agreement with the experimental herringbone results of Fig. 2). Second, there is a slight decrease in the amount of binding in the regions of the microchannel where the herringbone microstructure sits above the base microchannel (demarcated by the black arrows along the length of the microchannel) compared to regions without the herringbone microstructures. This reduction in the amount of bound SA can be attributed to a reduction in the local velocity due to the increased depth of the microchannel. The model results also show a reduction in the SA binding very near the sidewalls, again due to a reduced fluid velocity of the no-slip condition at the walls of the device.

The model results of the reverse herringbone microchannel (rightmost column of Fig. 4) show several interesting features. First, as in the case of the herringbone microchannel, there is a reduction in SA binding in the regions of the surface above which the herringbone microstructure is located. Second, the model results clearly show a greater amount of SA bound at the midline of the channel than was suggested by the experimental data. And finally, the model results show, as in the cases of the other two microchannel configurations, a reduction in SA binding very near the sidewalls, again due to a reduced fluid velocity there.

An important point is that in an alternative herringbone geometry, such as the staggered herringbone presented by Stroock *et al.*[24], the protein surface binding pattern would differ from the one presented here, *i.e.* the binding pattern is geometry-dependent.

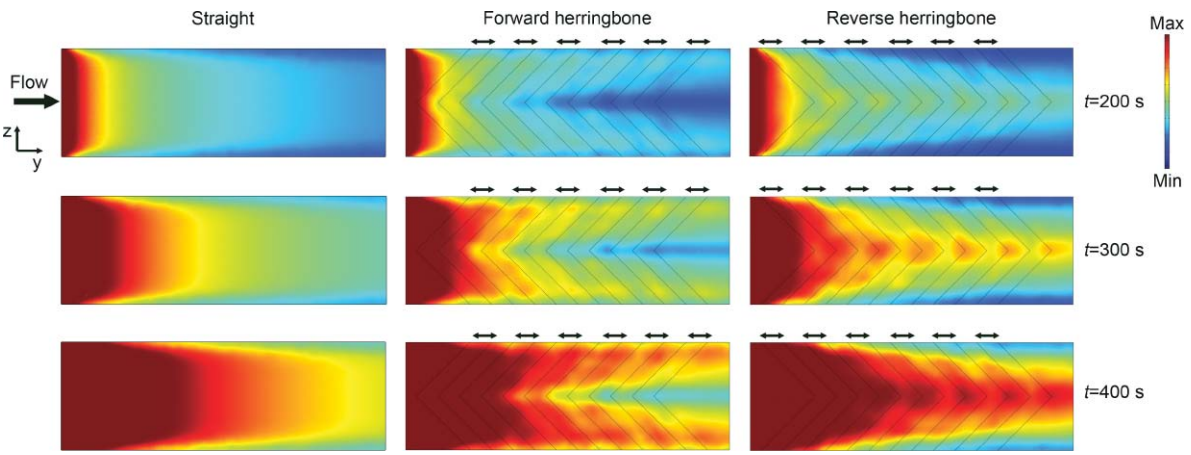

Fig. 4 Model surface concentration profile of bound SA (mol m^{-2}) in each microchannel over time. The arrows indicate the deepest portion of the channel where the herringbone microstructure was present. The maximum and minimum concentrations were 3.99×10^{-8} and 0 mol m^{-2} respectively. Note the very dramatic differences in the spatial patterns of surface binding.

Bulk concentration profile of the protein in the microchannel

The model can also give insight into the velocity profile (see the ESI†) and the concentration profile of SA within the microchannel (Fig. 5), which together lead to the spatial variations in the binding patterns of SA in the microchannels. As expected, when an assay in a straight microchannel (Fig. 5a) operates in the mass-transport-limited regime, a "depletion zone" very quickly forms above the binding surface as the SA in those regions binds to the surface. This leads to a reduction in the capture efficiency of SA in regions of the binding surface further downstream (*y*-dimension) as evidenced in Fig. 2.

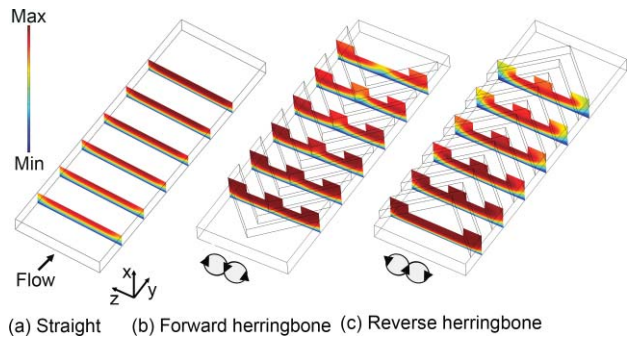

Fig. 5 Model concentration profile of SA in each microchannel (mol m^{-3}). The maximum and minimum concentrations were 40 and 0 nM respectively. The concentration profile of SA in each microchannel is consistent with the resulting spatial distribution of bound SA presented for each case in Fig. 2.

The clockwise and counterclockwise recirculation flows introduced by the herringbone microchannel alter the bulk concentration profile of SA (Fig. 5b, see ESI for a detailed analysis of the velocity profile†) and, in turn, affect the 2-dimensional surface binding profile (Fig. 2). At the start of the device, solution from the top of the microchannel which is not depleted of SA is pulled toward the surface at the sidewalls of the device. Then, the transverse flow (*z*-dimension) sweeps the SA across the surface towards the midline of the channel, in the process depleting the solution of SA as it binds to the surface. This gives rise to two symmetric regions of increased SA surface binding about the midline of the channel (Fig. 2). At the channel midline, the solution is now depleted of SA—resulting in a reduction in SA binding at the midline of the channel (Fig. 2). The solution is then swept upward to the top of the herringbone microstructure, across the herringbone microstructure, and is once again brought to the sidewalls of the microchannel. This cycle of recirculation continues down the length of the herringbone microchannel. The recirculation initially gives rise to a column of solution depleted of SA at the midline of the microchannel, as shown in Fig. 5b, which is eventually swept around the device and again toward the binding surface. The result is the decreased binding of SA along the midline of the microchannel. Eventually, the solution near the walls will become depleted of SA, thereby giving rise to two cores of solution with concentrated SA at the center of the recirculation zones.

In the reverse herringbone microchannel (Fig. 5c), the handednesses of the recirculating flows is reversed. At the midline of the microchannel, the solution from the herringbone microstructure flows toward the surface and then sweeps across the surface (*z*-dimension) where SA binds. As the solution sweeps across the binding surface it becomes depleted of SA as it approaches the sidewalls. As a consequence, increased binding of SA occurs along the midline of the microchannel and binding is reduced near the sidewalls (Fig. 4).

Total binding of SA

A critical question in the analysis of the herringbone microchannel and reverse herringbone microchannel is whether more SA binds to the surface as in the case of the straight microchannel. Model results for the spatially averaged binding rate within a region 1.5 mm in length (Fig. 6) indicate that there is no difference in the total binding of SA between the herringbone, reverse herringbone and straight microchannels over a timescale of 500 s. The model results are consistent with those reported by Golden *et al.*[9] which indicate that there was no measurable difference in the amount of material bound at the start of the mixer microchannel and the straight microchannel in their microfluidic assay. Previous experimental demonstrations of significant increases in total binding in a herringbone microchannel *versus* a straight microchannel were recorded at much greater downstream distances. For example, Golden *et al.*[9] presented modest increases in the binding signal at locations from 20 to 140 mm downstream, approximately 10 to 90 times the distance explored by the current model. Simulation of microchannel geometries larger than the modeled geometry were not feasible due to limitations of computational power.

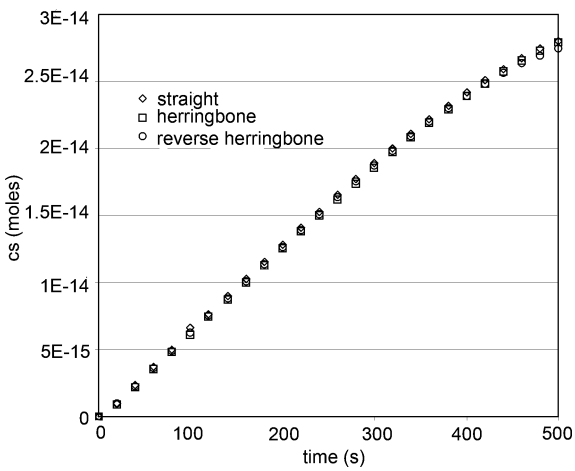

Fig. 6 Model results for the forward herringbone, reverse herringbone, and straight microchannel configurations show similar average rates of SA binding within a region 1.5 mm in length over a timescale of 500 s.

In the model system of the current study, the fact that the amount of SA bound to the surface of the herringbone microchannel is not significantly greater than the amount bound to the surface of the straight microchannel in regions of the binding patch immediately downstream of the start is most likely due to the relative magnitudes of the velocity components. If the transverse velocity (*z*-dimension, Fig. 1) and the velocity to and from the binding surface (*x*-dimension, Fig. 1) are significant relative to the downstream velocity (*y*-dimension, Fig. 1), the recirculation of the fluid would result in a significant number

of rotations over the length of the binding patch of interest and a relative increase in the amount of bound SA would occur. On the other hand, if the transverse velocity and velocity to and from the binding surface are very small relative to the downstream velocity, the recirculation would occur only over a large downstream length compared to the length of the binding patch of interest. In this scenario, *i.e.* the case for the modeled herringbone microchannel (see ESI for further details†), a distance longer than 1.5 mm would be required for the solution to circulate from the top of the herringbone microchannel to the binding surface, *i.e.* for there to be a significant increase in SA binding in the herringbone microchannel as compared to a straight microchannel.

Conclusions

This work represents the first attempt to analyze the spatio-temporal binding of a protein to a surface within a herringbone microchannel and a reverse herringbone microchannel. We have shown, using experimental and model results, that the transverse circulation of the protein solution within the microchannels gives rise to unique 2-dimensional surface binding profiles of SA. In the herringbone microchannel there was a significant increase in the surface binding of protein near the sidewalls and a reduction in protein binding at the midline of the microchannel. The surface binding pattern in the reverse herringbone microchannel was the inverse of that in the herringbone microchannel—an increase in SA binding along the midline of the channel and a reduction in binding near the sidewalls. The experimental surface binding profiles of SA showed strong qualitative agreement with model results. The model results of the concentration profile of SA within the bulk of the device coupled with the velocity profiles (see ESI†) further illustrate that the unique binding profile of SA was a result of two spiraling flows down the length of the microchannel. Given the distinctive surface binding profile of SA, the herringbone microchannel may be a useful method to pattern molecules on a surface passively.

Comparison of model results for the straight microchannel, herringbone microchannel and reverse herringbone microchannel indicated that the recirculation did not increase the amount of SA bound over time, consistent with previous experimental findings.[9]

With the development of a computational model that shows a strong qualitative correlation with experimental results, future work may include the computational optimization of the herringbone microchannel geometry for mixing solutions in the bulk as well as the optimization of the binding of molecules to the surface of the microchannel by altering any number of variables including the flow rate, herringbone depth, width of the herringbone, distance between herringbones, channel width, and relative depth of the herringbone microstructure *versus* the depth of the base microchannel. The model could also be used to explore other assay designs. Of particular interest would be analytes that have smaller diffusion coefficients than a protein molecule (*e.g.* microspheres), since it is likely that the herringbone microchannel will produce more significant increases in the surface binding rates compared to a straight channel under more mass-transport-limited conditions.

Acknowledgements

The thiol surface-patterning method was developed and optimized by Dr Kjell Nelson and Neil Geisler; Dr Roya Sabeti and Dr Elena Garcia assisted with the microfabrication of the two-layer SU8 molds in our laboratory. Dr Albert Folch generously allowed access to oxygen plasma equipment. This work was completed under the support of a NIH training grant (1 T32 GM065098–01A1) and a grant from NIDCR (1U01 DE014971).

Notes and references

1 P. von Lode, *Clin. Biochem.*, 2005, **38**, 591–606.
2 P. Yager, T. Edwards, E. Fu, K. Helton, K. Nelson, M. R. Tam and B. H. Weigl, *Nature*, 2006, **442**, 412–418.
3 M. Toner and D. Irimia, *Annu. Rev. Biomed. Eng.*, 2005, **7**, 77–103.
4 C. D. Chin, V. Linder and S. K. Sia, *Lab Chip*, 2007, **7**, 41–57.
5 A. M. Dupuy, S. Lehmann and J. P. Cristol, *Clin. Chem. Lab. Med.*, 2005, **43**, 1291–1302.
6 H. Becker and C. Gartner, *Electrophoresis*, 2000, **21**, 12–26.
7 H. Becker and L. E. Locascio, *Talanta*, 2002, **56**, 267–287.
8 H. A. Stone and S. Kim, *AIChE J.*, 2001, **47**, 1250–1254.
9 J. P. Golden, T. M. Floyd-Smith, D. R. Mott and F. S. Ligler, *Biosens. Bioelectron.*, 2007, **22**, 2763–2767.
10 S. K. Yoon, G. W. Fichtl and P. J. A. Kenis, *Lab Chip*, 2006, **6**, 1516.
11 D. A. Zubtsov, S. M. Ivanov, A. Y. Rubina, E. I. Dementieva, V. R. Chechetkin and A. S. Zasedatelev, *J. Biotechnol.*, 2006, **122**, 16–27.
12 M. Sigurdson, D. Dazhi Wang and C. Meinhart, *Lab Chip*, 2005, **5**, 1366.
13 M. K. McQuain, K. Seale, J. Peek, T. S. Fisher, S. Levy, M. A. Stremler and F. R. Haselton, *Anal. Biochem.*, 2004, **325**, 215–226.
14 J. Liu, B. A. Williams, R. M. Gwirtz and B. J. a. S. Q. Wold, *Angew. Chem., Int. Ed.*, 2006, **45**, 3618.
15 F. Raynal, F. Plaza, A. Beuf, P. Carriere, E. Souteyrand, J. R. Martin, J. P. Cloarec and M. Cabrera, *Phys. Fluids*, 2004, **16**, L63–L66.
16 F. Raynal, A. Beuf, F. Plaza, J. Scott, P. Carriere, M. Cabrera, J. P. Cloarec and E. Souteyrand, *Phys. Fluids*, 2007, **19**, 17112.
17 J. M. Hertzsch, R. Sturman and S. Wiggins, *Small*, 2007, **3**, 202–218.
18 M. Herrmann, T. Veres and M. Tabrizian, *Lab Chip*, 2006, **6**, 555–560.
19 M. A. Bynum and G. B. Gordon, *Anal. Chem.*, 2004, **76**, 7039–7044.
20 N. B. Adey, M. Lei, M. T. Howard, J. D. Jensen, D. A. Mayo, D. L. Butel, S. C. Coffin, T. C. Moyer, D. E. Slade, M. K. Spute, A. M. Hancock, G. T. Eisenhoffer, B. K. Dalley and M. R. McNeely, *Anal. Chem.*, 2002, **74**, 6413–6417.
21 K. A. Ghaleb, K. Stephan, P. Pittet, R. Ferrigno and J. Georges, *Appl. Spectrosc.*, 2006, **60**, 564–567.
22 T. M. Floyd-Smith, J. P. Golden, P. B. Howell and F. S. Ligler, *Microfluid. Nanofluid.*, 2006, **2**, 180–183.
23 R. A. Vijayendran, K. M. Motsegood, D. J. Beebe and D. E. Leckband, *Langmuir*, 2003, **19**, 1824–1828.
24 A. D. Stroock, S. K. W. Dertinger, A. Ajdari, I. Mezic, H. A. Stone and G. M. Whitesides, *Science*, 2002, **295**, 647–651.
25 P. B. Howell, Jr, D. R. Mott, S. Fertig, C. R. Kaplan, J. P. Golden, E. S. Oran and F. S. Ligler, *Lab Chip*, 2005, **5**, 524–530.
26 H. Sato, S. Ito, K. Tajima, N. Orimoto and S. Shoji, *Sens. Actuators, A*, 2005, **119**, 365–371.
27 B. P. Nelson, T. E. Grimsrud, M. R. Liles, R. M. Goodman and R. M. Corn, *Anal. Chem.*, 2001, **73**, 1–7.
28 B. P. Nelson, A. G. Frutos, J. M. Brockman and R. M. Corn, *Anal. Chem.*, 1999, **71**, 3928–3934.
29 E. Fu, J. Foley and P. Yager, *Rev. Sci. Instrum.*, 2003, **74**, 3182–3184.
30 K. E. Nelson, L. Gamble, L. S. Jung, M. S. Boeckl, E. Naeemi, S. L. Golledge, T. Sasaki, D. G. Castner, C. T. Campbell and P. S. Stayton, *Langmuir*, 2001, **17**, 2807–2816.
31 L. S. Jung, K. E. Nelson, P. S. Stayton and C. T. Campbell, *Langmuir*, 2000, **16**, 9421–9432.
32 Y. Xia and G. M. Whitesides, *Angew. Chem., Int. Ed.*, 1998, **37**, 550–575.
33 D. C. Duffy, J. C. McDonald, O. J. A. Schueller and G. M. Whitesides, *Anal. Chem.*, 1998, **70**, 4974–4984.

34 K. E. Nelson, J. O. Foley and P. Yager, *Anal. Chem.*, 2007, **79**, 3542–3548.
35 E. Fu, T. Chinowsky, J. Foley, J. Weinstein and P. Yager, *Rev. Sci. Instrum.*, 2004, **75**, 2300–2304.
36 *Handbook for FEMLAB Transport Phenomena Course*, COMSOL, 2003, pp. 38–48.
37 J. O. Foley, K. E. Nelson, A. Mashadi-Hossein, B. A. Finlayson and P. Yager, *Anal. Chem.*, 2007, **79**, 3549–3553.
38 J. Spinke, M. Liley, F. J. Schmitt, H. J. Guder and K. L. W. J. Angermaier, *J. Chem. Phys.*, 1993, **99**, 7012.
39 P. C. Weber, J. J. Wendoloski, M. W. Pantoliano and F. R. Salemme, *J. Am. Chem. Soc.*, 1992, **114**, 3197.
40 B. R. Munson, D. F. Young and T. H. Okiishi, *Fundamentals of Fluid Mechanics*, John Wiley and Sons, Inc., New York, 4th edn, 2002.
41 B. A. Finlayson, *Non-linear Analysis in Chemical Engineering*, McGraw-Hill College, New York, 1980.

